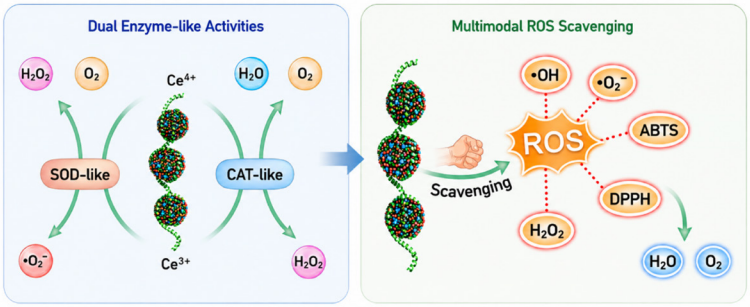
BIO Integration

Original Article

A Synergistically Enhanced Cerium-Based Nanozyme: Multi-Effect Strategy for Diabetic Wound Healing

Graphical abstract



Highlights

- Ce@BSA-TA was constructed *via* BSA-mediated biomineralization and tannic acid functionalization.
- Ce^{3+}/Ce^{4+} redox cycling provides SOD- and CAT-mimetic activities for multimodal ROS scavenging.
- Ce@BSA-TA alleviates oxidative stress and regulates the inflammatory wound microenvironment.
- The combined antioxidative and anti-inflammatory effects promote tissue regeneration and diabetic wound healing.

Authors

Yuhui Sun, Hongda Ma, Yan Xu, Yuan Cui, Leijiao Li, Xincui Shi, Xiangru Feng, Alexander A. Titov and Wenliang Li

Correspondence

lileijiao@cust.edu.cn (L. Li);
titov-aa@rudn.ru (A. A. Titov);
wenliangl@ciac.ac.cn (W. Li)

In brief

Ce@BSA-TA is a cerium-based nanozyme with SOD- and CAT-mimetic activities that facilitates multimodal ROS scavenging through Ce^{3+}/Ce^{4+} redox cycling. By alleviating oxidative stress and regulating the inflammatory microenvironment, Ce@BSA-TA creates favorable conditions for tissue regeneration and diabetic wound healing.

©2026 The Authors. Creative Commons Attribution 4.0 International License

Original Article

BIO Integration

A Synergistically Enhanced Cerium-Based Nanozyme: Multi-Effect Strategy for Diabetic Wound Healing

Yuhui Sun[1], Hongda Ma[1], Yan Xu[1], Yuan Cui[1], Leijiao Li[1,*], Xincui Shi[1], Xiangru Feng[2], Alexander A. Titov[3,*] and Wenliang Li[1,4,*]

Abstract

Objective: Diabetic wound healing is frequently impaired by excessive oxidative stress, persistent inflammation, and insufficient tissue regeneration. The aim of this study was to develop a multifunctional cerium-based nanozyme capable of regulating the oxidative and inflammatory microenvironments to promote diabetic wound repair.

Methods: A tannic acid–functionalized cerium-based nanocomposite (Ce@BSA-TA) was constructed *via* bovine serum albumin (BSA)-mediated biomineralization followed by tannic acid (TA) modification. The physicochemical properties and enzyme-mimetic activity of Ce@BSA-TA were characterized, and its ability to scavenge reactive oxygen species (ROS) was evaluated. Cytoprotective and pro-migratory effects were investigated *in vitro* under high-glucose–associated oxidative stress. A diabetic mouse model with full-thickness skin wounds was used to evaluate wound healing, inflammatory regulation, angiogenesis, and collagen deposition.

Results: Benefiting from the Ce^{3+}/Ce^{4+} redox cycle, Ce@BSA-TA exhibited superoxide dismutase (SOD)- and catalase (CAT)-mimetic activities and effectively scavenged superoxide anions ($O_2^{\bullet-}$) and hydrogen peroxide (H_2O_2). Ce@BSA-TA alleviated intracellular oxidative stress, protected cells from oxidative damage, and promoted fibroblast migration *in vitro*. In diabetic wounds, Ce@BSA-TA reduced oxidative stress and pro-inflammatory cytokine expression, promoted macrophage polarization toward the M2 phenotype, and enhanced angiogenesis and collagen deposition, which collectively accelerated wound closure.

Conclusion: Ce@BSA-TA integrates ROS scavenging and immunomodulatory activities to improve the hostile microenvironment of diabetic wounds and promote tissue repair. Our study findings support the potential of multifunctional cerium-based nanozymes as a therapeutic strategy for the management of chronic diabetic wounds.

Keywords

Cerium, Diabetic wound healing, Immunomodulation, Nanozyme, ROS scavenging.

[1]School of Chemistry and Environmental Engineering, Changchun University of Science and Technology, Changchun 130022, China

[2]School of Life Science and Technology, Changchun University of Science and Technology, Changchun 130022, China

[3]Organic Chemistry Department, Science Faculty, Peoples' Friendship University of Russia Named After Patrice Lumumba (RUDN University), Moscow 117198, Russian Federation

[4]Jilin Medical University, Jilin 132013, China

*Correspondence to: Leijiao Li, School of Chemistry and Environmental Engineering, Changchun University of Science and Technology, Changchun 130022, China. E-mail: lileijiao@cust.edu.cn; Alexander A. Titov, Organic Chemistry Department, Science Faculty, Peoples' Friendship University of Russia Named After Patrice Lumumba (RUDN University), Moscow 117198, Russian Federation. E-mail: titov-aa@rudn.ru; Wenliang Li, Jilin Medical University, Jilin 132013, China. E-mail: wenliangl@ciac.ac.cn

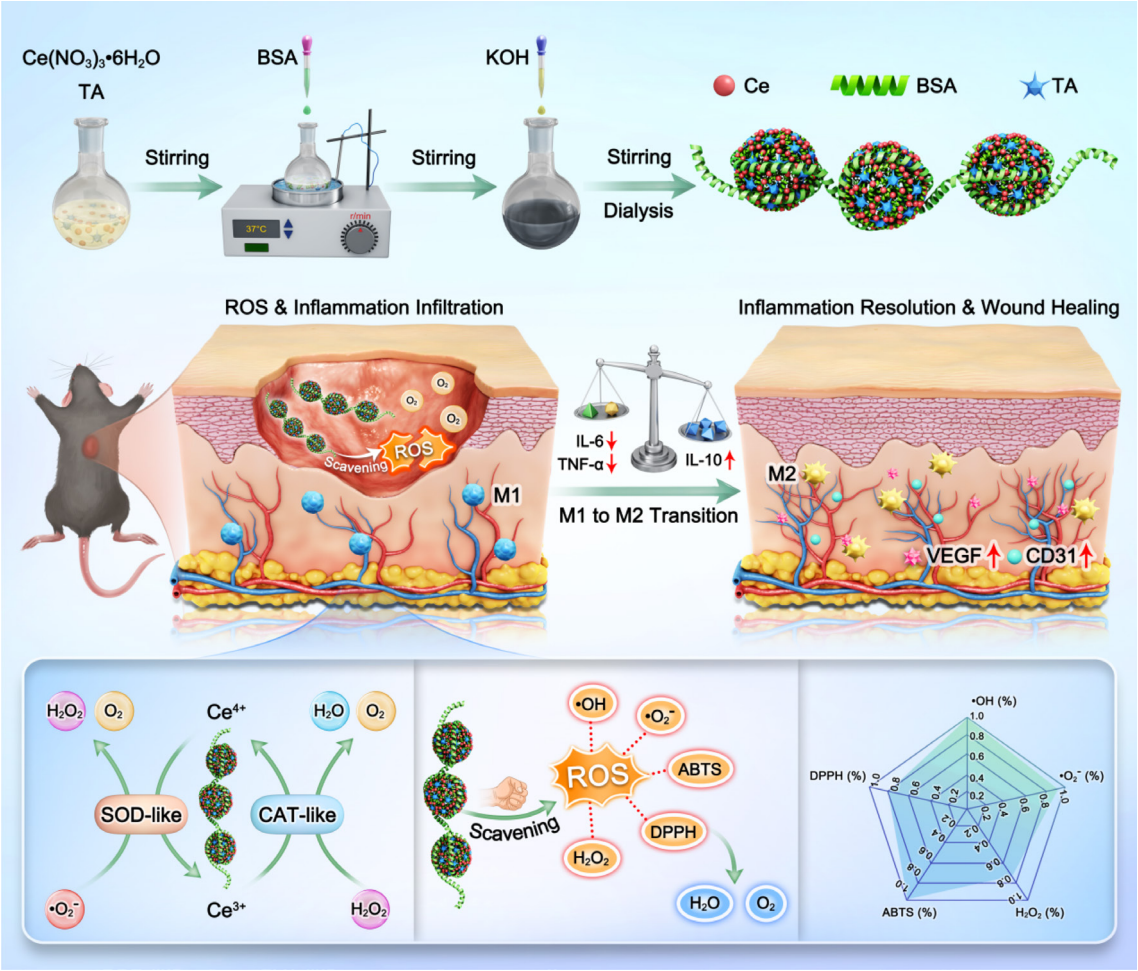
Received: July 9 2026
Revised: August 5 2026
Accepted: September 1 2026
Published Online: November 1 2026

Available at: https://bio-integration.org/

Introduction

Diabetes is one of the most prevalent chronic diseases worldwide and often leads to diabetic nonhealing wounds, which is a complication that puts patients at significant risk of amputation and mortality [1]. Evidence indicates that pathological accumulation of reactive oxygen species (ROS) is a core mechanism hindering the healing of diabetic wounds. ROS accumulation interferes with key biological processes for wound repair *via* oxidative stress [2]. The high-glucose microenvironment in diabetes disrupts the mitophagy mechanism, which leads to abnormal accumulation of dysfunctional mitochondria [3, 4]. This in turn triggers an increase in ROS production alongside a decrease in ATP synthesis [5, 6]. This metabolic dysfunction not only impairs angiogenesis by downregulating the expression of vascular endothelial growth factor (VEGF) but also disrupts the balance of macrophage phenotypes, which further hinders the wound healing process [7]. Although M1 macrophages eliminate pathogens by secreting ROS and proteases in the early stage of inflammation, persistent oxidative stress can hinder their transformation to promote repair of the M2 phenotype, which results in a chronic inflammatory microenvironment that inhibits epithelization and angiogenesis [8, 9].

To address the multiple pathological mechanisms described above, we prepared a bovine serum albumin (BSA)-coated tannic acid (TA)–cerium nanozyme *via* a method that combined biomineralization



Scheme 1 Schematic illustration of the synthesis of Ce@BSA-TA and the mechanism responsible for enhanced multimodal ROS scavenging and diabetic wound healing.

with self-assembly (Ce@BSA-TA; **Scheme 1**). This nanozyme treatment platform has three functional characteristics: (1) multimodal ROS scavenging ability (efficient scavenging of hydroxyl radicals, superoxide anions, and hydrogen peroxide); (2) promotion the macrophage transformation to the M2 phenotype (downregulation of CD86, TNF-α and IL-6 pro-inflammatory factors; upregulation of CD206 and IL-10 anti-inflammatory factors); and (3) significant enhancement of angiogenesis *via* upregulation of the VEGF pathway and CD31 levels. This study provides an innovative solution for breaking the vicious cycle of oxidative stress–healing disruption in diabetic wounds, and provides a theoretical basis for the design and application of ROS-regulating nanomaterials for the treatment of chronic wounds.

Materials and methods

Materials

$Ce(NO_3)_3{\cdot}6H_2O$ (99.5%), TA, riboflavin, potassium chloride, potassium persulfate, potassium dihydrogen phosphate, titanium sulfate, sodium glacial acetate, glacial aceic acid, disodium hydrogen phosphate (Na_2HPO_4), DMPO, Potassium ferricyanide, trichloroacetic acid, DMEM, FBS, penicillin-streptomycin, DCFH-DA, L929 cell line, Streptozotocin, Avertin, Triton X-100, Tris, Tween 20, the primary antibodies, DAPI, and paraformaldehyde were purchased from Shanghai Aladdin Biochemical Technology (Shanghai, China). Avridine and BSA were purchased from Shanghai Yuanye Biotechnology (Shanghai, China). Folic acid (FA) was purchased from Anhui Zesheng Technology (Anqing, China). L-Methionine, nitroblue tetrazolium chloride (NBT), 2,2-diphenyl-1-picrylhydrazyl hydrate (DPPH), 2,4,6-tripyridyl triazine (TPTZ), and 2,2′-azino-bis(3-ethylbenzothiazoline-6-sulfonic acid) diamine salt (ABTS) were purchased from Shanghai McLean Biochemical Technology (Shanghai, China). Sodium salicylate was purchased from Tianjin Yongda Chemical. CCK-8 was purchased from Shanghai Tongwei Industrial (Shanghai, China). Reagents (Tianjin, China). Hydrogen peroxide was purchased from Nanjing Chemical Reagents (Nanjing, China). Ferrous sulfate heptahydrate was purchased from Shanghai Myrill Biochemical Technology (Shanghai, China). Methylene blue (MB) was purchased from the Beijing Institute of Chemical Reagents (Beijing, China). Anhydrous ethanol and methanol were purchased from Tianjin Fuyu Fine Chemicals (Tianjin, China). Ethylenediamine tetra-acetic acid (EDTA) was purchased from Tianjin Guangfu Technology Development (Tianjin, China). Iron chloride was purchased from Beijing Chemical Industry (Beijing, China). Saline was purchased

from Liaoning Minkang Pharmaceuticals (Dalian, China). Medical disinfection ethanol was purchased from Shandong Dexinkang Medical (Dezhou, China). Potassium hydroxide (KOH), hydrochloric acid, ammonia, hydrogen peroxide, absolute ethanol, neutral gum, and xylene were purchased from China Pharmaceutical Group Chemical Reagents (Shanghai, China). Masson staining kits and hematoxylin–eosin (H&E) staining solutions were purchased from Wuhan Servicebio Biotechnology (Wuhan, China). $[Ru(dpp)_3]Cl_3$ was purchased from Shanghai Maokang Biotechnology (Shanghai, China). Calcein AM and propidium iodide (PI) were purchased from Thermo Fisher Scientific (Shanghai, China).

Transmission electron microscopy (TEM): JEM-2100F (JEOL, Tokyo, Japan) transmission electron microscopy was used to analyze the microscopic morphology and nano-size of cerium-based nanomaterials. X-ray diffraction (XRD): Using Shimadzu XRD-6100 (Shimadzu, Kyoto, Japan) to test 10°–80°, the scanning speed was 2° min−1 and the structural characteristics of cerium-based nanomaterials were studied. X-ray photoelectron spectroscopy (XPS): The PHI 5000 Versa Probe (Physical Electronics, Chanhassen, MN, USA) spectrometer was used to analyze the elemental composition of the samples. Fourier transform infrared spectroscopy (FT-IR): The infrared absorption of the sample was collected in the range of 300–4000 cm−1 using the Bruker TENSOR II (Bruker Optik GmbH, Ettlingen, Germany) infrared spectrometer to analyze its functional groups. Ultraviolet-visible absorption spectroscopy (UV-Vis) was used to analyze the sample composition using Shimadzu UV3600 (Shimadzu, Kyoto, Japan) ultraviolet spectrophotometer to determine the absorption characteristics of molecules in the 200–600 nm region.

Thermogravimetric analysis (TGA): The thermal stability of the sample in a nitrogen atmosphere was studied using a simultaneous thermogravimetric analyzer (SDT6000TG) at a heating rate of 10 °C min−1. Electron paramagnetic resonance (EPR) was used to analyze the behavior of electron spin by Magnettech's MS-5000 X (Magnettech, Berlin, Germany) spectrometer, and the free radical scavenging performance of the sample was studied. All experiments used Milli-Q ultrapure water (18.25 MΩ•cm). The scavenging ability of hydroxyl radicals was detected by the salicylic acid method, EPR, and methylene blue (MB) spectrophotometry. The scavenging effect of superoxide anion was detected by tetrazolium blue (NBT) illumination method. The scavenging ability of hydrogen peroxide was detected by the titanium sulfate scavenging method. Other detailed experimental contents can be found in the supplementary materials.

Preparation of Ce@BSA

$Ce(NO_3)_3{\cdot}6H_2O$ (0.25 mL, 0.1 mol/L) and BSA (4.5 mL, 25 mg/mL) were added to a round-bottomed flask and mixed, and the flask was placed in a water bath at a specific temperature. Then 1 mol/L KOH solution (approximately 0.3 mL) was added dropwise to adjust the pH to approximately 13. During the reaction, the color of the solution changed from milky white to pale yellow. On completion of the reaction, the product was transferred into a dialysis bag (molecular weight cutoff: 1000 Da) and dialyzed against deionized water for 24 h. After dialysis, the product was isolated *via* centrifugation in an ultrafiltration tube at 4000 rpm for 15 min and washed multiple times with deionized water to remove impurities. Finally, the purified sample was lyophilized to obtain the final Ce@BSA product.

Preparation of Ce@BSA-TA and Ce@BSA-FA

To prepare Ce@BSA-TA, 0.1 mol/L $Ce(NO_3)_3{\cdot}6H_2O$ (0.25 mL) was mixed with 0.1 mol/L aqueous TA solution (0.25 mL) under continuous stirring for 12 h to allow the formation of a stable complex. Then 4.5 mL of BSA (25 mg/mL) was added and the mixture was incubated in a water bath at 37 °C to ensure thorough mixing. The pH of the reaction system was adjusted to approximately 13 using 1 mol/L KOH solution, during which the color of the solution changed from milky white to black. The reaction was maintained under constant temperature and stirring until completion. The resulting solution was transferred into a dialysis bag (molecular weight cutoff: 1000 Da) and purified against deionized water for 24 h. The dialyzed suspension was concentrated using a 10-kDa ultrafiltration centrifugal tube at 4000 rpm. The precipitate was washed three times with deionized water to remove residual reagents. After vacuum lyophilization for 24 h, the final product was obtained as a black solid powder. For synthesis of the FA-containing analogue, the TA was replaced with an equimolar amount of FA while keeping all other experimental parameters and procedures identical.

Hydroxyl radical scavenging activity

The hydroxyl radical (·OH) scavenging activity was determined using the salicylic acid method. In brief, 1 mL of $FeSO_4$ solution (5 mmol/L), 1 mL of H_2O_2 (2%), 1 mL of ethanolic salicylic acid solution (2.5 mmol/L), and 1 mL of deionized water were mixed and incubated in a water bath at 37 °C for 30 min; this was designated the positive control. For the sample groups, various concentrations of the product samples (6.25, 12.5, 25, and 50 μg/mL) were added to the aforementioned mixture instead of deionized water, and the mixtures were incubated at 37 °C for 30 min. These were labeled as the Ce@BSA, Ce@BSA-FA, and Ce@BSA-TA groups according to the sample added. After the reaction, the absorbance of each solution was measured at 510 nm using a UV-Vis spectrophotometer. The absorbance of the positive control was recorded as A_0, and the absorbance of the sample groups as A_1. Each experiment was performed in triplicate to compare the changes in absorbance. The ·OH scavenging rate (%) was calculated according to the following equation:

$$\text{Scavenging rate (\%)} = \left[1 - \frac{A_1 - A_0}{A_0}\right] \times 100\%. \quad (1)$$

Evaluation of ROS scavenging ability *via* electron paramagnetic resonance spectroscopy

Electron paramagnetic resonance (EPR) spectroscopy was used to evaluate the radical scavenging performance of the cerium-based nanomaterials, with 5,5-dimethyl-1-pyrroline-*N*-oxide (DMPO) Shanghai Aladdin Biochemical Technology (Shanghai, China). as the spin-trapping agent. The DMPO concentration was maintained at 100 mmol/L, and the concentration of the cerium-based nanomaterials was set at 50 μg/mL. Spectra were recorded on an EPR spectrometer after co-incubating the nanomaterials with DMPO for incubation times of 0, 15, and 30 min to determine their dynamic ROS scavenging ability.

MB assay for evaluation of ·OH scavenging ability

A solution containing MB alone (45 μg/mL) was used as a negative control. The positive control was prepared by adding 1 mL of H_2O_2 (1.5 mmol/L) and 1 mL of $FeSO_4$ (1.5 mmol/L) to MB solution (45 μg/mL), followed by incubation in a water bath at 37 °C for 30 min. For the experimental groups, different cerium-based nanomaterials (200 μg/mL) were added to the positive control mixture and reacted at 37 °C for 30 min. UV-Vis spectra were then recorded in the range 400–900 nm. The ·OH scavenging ability of the cerium-based nanomaterials was evaluated by comparing the change in absorbance at 664 nm. All solutions were freshly prepared before use and stored in the dark to avoid light exposure.

NBT assay for evaluation of $\cdot O_2^-$ scavenging activity

The $\cdot O_2^-$ scavenging activity was evaluated using the NBT method. Riboflavin (100 μmol/L), methionine (39 mmol/L), EDTA (1 mmol/L), and sample solutions (1 mg/mL) were prepared using 2× phosphate-buffered saline (PBS; pH 7.4), while the NBT solution (1.125 mmol/L) was prepared in absolute ethanol. The reaction mixtures included a positive control, a negative control, and Ce@BSA, Ce@BSA-FA, and Ce@BSA-TA samples. Under dark conditions, a spherical 36-W LED lamp was used as the light source, positioned at a distance of 1 cm from the sample vials. The positive control was illuminated for 10 min and then its absorbance at 560 nm was measured and recorded as A_0. The negative control was kept in the dark for 10 min and its absorbance at 560 nm was then recorded as A_2. The samples were illuminated for 10 min and their absorbance at 560 nm was then recorded as A_1. Each experiment was performed in triplicate, and the average values were used for analysis. The $\cdot O_2^-$ scavenging rate (%) was calculated using the following equation:

$$\text{Scavenging rate (\%)} = \left[1-\frac{A_1-A_2}{A_2-A_0}\right]\times 100\%. \quad (2)$$

Evaluation of H_2O_2 scavenging and O_2 production

H_2O_2 (100 mmol/L) and cerium-based nanomaterial solutions (1 mg/mL for Ce@BSA, Ce@BSA-FA, and Ce@BSA-TA) were prepared. A dissolved oxygen (DO) Thermo Fisher Scientific (Shanghai, China) meter was switched on, preheated, and calibrated according to the manufacturer's instructions. This instrument was purchased from Thermo Fisher Scientific (Shanghai, China). The reaction systems were divided into a control group and experimental groups (designated as Ce@BSA, Ce@BSA-FA, and Ce@BSA-TA). The initial DO content in each system was measured. Then 30 mL of 100 mmol/L H_2O_2 was added and the DO level was recorded after 10 min. The H_2O_2 scavenging efficiency of the cerium-based nanomaterials was evaluated by comparing DO levels between the experimental and control groups.

The H_2O_2 scavenging ability was re-evaluated using titanium sulfate. Specifically, 1.33 mL of 24% $Ti(SO_4)_2$ was dissolved in 50 mL of deionized water containing 8.33 mL of sulfuric acid. For the control group, 2 mL of PBS buffer, 100 μL of $Ti(SO_4)_2$ solution, and 1 mL of 1 mmol/L H_2O_2 were mixed thoroughly and allowed to react for 30 min. For the experimental groups, the same volumes of these reagents were mixed with a specific concentration of the sample solution and allowed to react for 30 min. After the reaction, the absorbance at 415 nm was recorded using a UV-Vis spectrophotometer for the control (A_0) and experimental (A_1) samples. Each experiment was performed in triplicate, and the average values were calculated. The H_2O_2 scavenging rate was determined according to the following equation:

$$\text{Scavenging rate (\%)} = \frac{A_1-A_0}{A_0}\times 100\%. \quad (3)$$

Determination of ABTS·$^+$ scavenging activity

The ABTS·$^+$ scavenging activity was measured according to a standard protocol. For the assay, 3 mL of ABTS working solution was mixed with 30 μL of either methanol (control) or the sample solution (experimental samples) and allowed to react in the dark for 30 min. After the reaction, the absorbance at 745 nm was measured using a spectrophotometer for the control (A_0) and experimental samples (A_1). Each measurement was performed in triplicate, and the results were averaged. The scavenging rate for ABTS·$^+$ was calculated using Equation (3).

DPPH· scavenging assay

A series of five sample vials was prepared, each containing 5 mL of DPPH solution (45.6 μg/mL) and 1 mL of 95% ethanol. One vial served as the blank control, while sample solutions were added to the others to reach final concentrations of 50, 100, 150, and 200 μg/mL. The mixtures were

thoroughly homogenized and allowed to react in the dark for 30 min. After the reaction, the absorbance was measured at 517 nm using a spectrophotometer for the control (A_0) and experimental (A_1) samples. Each experiment was performed in triplicate, and the average values were calculated for analysis.

Determination of the total reducing power

The total reducing power was evaluated using the potassium ferricyanide reduction method. In brief, 0.5 mL of deionized water was mixed with 2.5 mL of PBS (pH 6.6) and 2.5 mL of 1% (w/v) $K_3Fe(CN)_6$. After incubation in a water bath at 50 °C for 20 min, 2.5 mL of 10% (w/v) trichloroacetic acid purchased from Shanghai Aladdin Biochemical Technology (Shanghai, China) was added and the mixture was then centrifuged at 1000 rpm for 10 min. A 5-mL aliquot of the resulting supernatant was collected, mixed with 5 mL of deionized water and 1 mL of 0.1% (w/v) ferric chloride ($FeCl_3$), homogenized, and allowed to stand for 2 min; this mixture was designated as the control. For the experimental groups, corresponding samples were added to the reaction mixture. The absorbance at 700 nm was measured using a spectrophotometer for the control (A_0) and experimental (A_1) groups. The total reducing power (%) was calculated according to the following equation:

$$\text{Total reducing power}\ (\%) = \frac{A_1 - A_0}{A_0} \times 100\%. \qquad (4)$$

Intracellular ROS scavenging activity

L929 cells were purchased from Thermo Fisher Scientific (Shanghai, China) cultured in Dulbecco's modified Eagle medium (DMEM) supplemented with 10% (v/v) fetal bovine serum (FBS) and 1% (v/v) penicillin–streptomycin (100 IU/mL) at 37 °C in a 5% CO_2 atmosphere. The cells were seeded into 24-well plates at a density of 3×10^4 cells per well. In the PBS group, cells were incubated with 2′,7-dichlorofluorescein diacetate (DCFH-DA) for 20 min in the dark. DMEM, FBS, penicillin–streptomycin and DCFH-DA were obtained from Shanghai Aladdin Biochemical Technology (Shanghai, China). For the H_2O_2 group, cells were stimulated with H_2O_2 after addition of PBS. After 1 h, the H_2O_2 medium was removed and the cells were washed three times with sterile PBS before incubation with DCFH-DA for 20 min in the dark, and subsequent washing three times with serum-free medium. For the experimental groups, a 2-mL aliquot of Ce@BSA, Ce@BSA-FA, or Ce@BSA-TA at various concentrations (3.125, 6.25, and 12.5 μg/mL) was added to the wells. The cells were then stimulated with H_2O_2 for 1 h. The medium containing the nanomaterials and H_2O_2 was removed and the cells were washed three times with sterile PBS, incubated with DCFH-DA for 20 min in the dark, and then washed three times with serum-free medium before imaging or measurement.

Intracellular oxygen evolution assay

L929 cells (1×10^5 cells/mL) were seeded into 96-well plates and incubated with $[Ru(dpp)_3]Cl_3$ was purchased from Shanghai Maokang Biotechnology (Shanghai, China) probes (dpp = 4,7-diphenyl-1,10-phenanthroline) for 30 min at 37 °C in a 5% CO_2 atmosphere. In the control group, 100 μL of cell culture medium containing 0.2 mmol/L H_2O_2 was added, and the fluorescence intensity was measured after a 30-min reaction. For the experimental groups, Ce@BSA, Ce@BSA-FA, and Ce@BSA-TA at various concentrations (3.125, 6.25, and 12.5 μg/mL) were added to the control systems. After 30 min of incubation, the intracellular fluorescence intensity was observed and recorded using an inverted fluorescence microscope.

Calcein-acetoxymethyl/propidium iodide staining

For dual staining with calcein-acetoxymethyl (calcein-AM) and propidium iodide (PI), L929 cells were seeded into 96-well plates (100 μL of cell suspension per well) and cultured until they adhered and reached an appropriate confluence. For the negative control group, the medium was replaced with freshly prepared complete DMEM. For the sample groups, cells were treated with Ce@BSA, Ce@BSA-FA, and Ce@BSA-TA solutions at various concentrations (3.125, 6.25, and 12.5 μg/mL). After 24-h incubation in a CO_2 incubator, the cells were stained using a Calcein-AM/PI Cytotoxicity Assay Kit were purchased from Thermo Fisher Scientific (Shanghai, China) according to the manufacturer's protocol. Live (green) and dead (red) cells were observed under an inverted fluorescence microscope, and the images captured were analyzed using Image J software.

In vitro cytotoxicity and cell viability assays

A suspension of L929 cells was thoroughly homogenized and 100-μL aliquots were seeded into each well of a 96-well plate, with three replicates for each sample and a negative control group. After initial culture, the medium was replaced with 100 μL of Ce@BSA and Ce@BSA-TA solutions (200 μg/mL). The plates were incubated for 3, 6, 12, and 24 h. Subsequently, 10% CCK-8 reagent was purchased from Shanghai Tongwei Industrial (Shanghai, China) added to each well and incubated for an additional 1 h. The absorbance was measured at 450 nm using a microplate reader, and average values were calculated.

L929 and NIH 3T3 cell suspensions (100 μL) were seeded into 96-well plates and cultured for 24 h to allow for cell adherence, after which the medium was replaced with fresh complete medium. For the experimental groups, cells were treated with various concentrations of Ce@BSA-TA and incubated in a 5% CO_2 atmosphere for 24 h. Subsequently, 3-(4,5-dimethylthiazol-2-yl)-2,5-diphenyltetrazolium bromide (MTT) solution was added to each well and incubated for an additional 4 h. MTT is reduced to purple formazan by

succinate dehydrogenase in the mitochondria of viable cells. The supernatant was removed from the wells, and 200 μL of dimethyl sulfoxide was added to each well to dissolve the formazan crystals. After 10-min incubation, the absorbance at 490 nm was measured using a microplate reader, and average values were calculated.

In vivo skin irritation assay

Filter paper discs (10 mm in diameter) were randomly assigned to five groups: a control group treated with PBS and experimental groups treated with Ce@BSA-TA at concentrations of 12.5, 25, 100, or 400 μg/mL. C57BL/6 mice were purchased from Shanghai Aladdin Biochemical Technology (Shanghai, China). randomly divided into five groups, and the hair on their dorsal skin was shaved. The pretreated filter papers were then applied firmly to the denuded dorsal skin of the mice. After 3 days of continuous exposure, the dorsal skin on each mouse was photographed and carefully examined to evaluate any potential allergic reactions or signs of irritation such as erythema or edema.

Hemolysis assay

Mouse blood was collected *via* retro-orbital bleeding into centrifugal tubes containing EDTA as an anticoagulant. Red blood cells (RBCs) were isolated *via* centrifugation, washed three times with PBS, and then resuspended in PBS. Subsequently, 0.2 mL of the RBC suspension was mixed with 0.8 mL of Ce@BSA-TA at various concentrations (100, 200, 300, 400, 500, and 600 μg/mL). Deionized water and PBS (0.8 mL each) were used to replace the Ce@BSA-TA for positive and negative controls, respectively. The mixtures were allowed to stand for 1 h and then centrifuged. The absorbance of the resulting supernatant was measured at 570 nm using a UV-Vis spectrophotometer for the positive control (A_2), negative control (A_0), and experimental samples (A_1). The hemolysis rate (%) was calculated using the following equation:

$$\text{Hemolysis rate } (\%) = \frac{A_1 - A_0}{A_2 - A_0} \times 100\%. \quad (5)$$

Establishment of a diabetic wound model in mice

C57BL/6 mice (weighing approximately 20 g) were fed a high-fat/high-sugar diet for 6 weeks until their body weight reached 30 g. Following a 12-h fast, the mice received intraperitoneal (i.p.) injections of streptozotocin (STZ; 100 mg/kg) purchased from Shanghai Aladdin Biochemical Technology (Shanghai, China) dissolved in citrate buffer (pH 4.5, prepared with citric acid and sodium citrate). After injections on three consecutive days, mice with a blood glucose level exceeding 16.7 mmol/L were identified as successful models of type II diabetes. The diabetic mice were then randomly grouped and numbered. The mice were anesthetized with i.p. Avertin (30 μL/g) purchased from Shanghai Aladdin Biochemical Technology (Shanghai, China) and the hair on their dorsal skin was removed. A circular, full-thickness skin excision wound (1 cm in diameter) was then established on the denuded dorsal area of each mouse to evaluate the efficacy of subsequent healing.

Treatment of diabetic wounds

The diabetic mouse models were randomly assigned to control and experimental groups (n = 6 mice per group at the beginning of the study). The control group was treated with sterile PBS, while the experimental groups received 30 μL of Ce@BSA-TA nanomaterial at various concentrations (12.5, 25, 100, and 400 μg/mL). Treatments were administered every 2 days. Wound closure was monitored by photographing the wounds at the time points indicated, and wound area was quantified using ImageJ software.

For tissue-based endpoint analyses, three mice from each group were euthanized on day 7, and the remaining three mice on day 14. Wound tissues collected at each time point were processed for histological, immunofluorescence, ROS, and enzyme-linked immunosorbent assay (ELISA) analyses. Tissue-based analyses at each time point were performed using samples from three biologically independent mice per group (n = 3).

H&E staining

Wound tissues were fixed in 4% paraformaldehyde, embedded in paraffin, and sectioned. After deparaffinization and rehydration, the sections were stained with hematoxylin and eosin (H&E) according to standard procedures. Histological changes were examined using an optical microscope.

Masson staining

Paraffin-embedded wound tissue sections were deparaffinized, rehydrated, and subjected to Masson's trichrome staining using standard procedures. Collagen deposition and distribution in wound tissues were evaluated using an optical microscope.

Immunofluorescence staining

Cells or tissue sections were fixed with 4% paraformaldehyde and permeabilized with 0.5% Triton X-100, Tris, Tween 20, the primary antibodies and DAPI were purchased from Shanghai Aladdin Biochemical Technology (Shanghai, China). The samples were then blocked with TBST buffer (Tris-buffered saline with Tween 20) containing 2% BSA for 30 min to minimize nonspecific binding. The sections were incubated overnight at 4 °C with primary antibodies against specific markers, including CD206, CD86, CD31, and VEGF. For intracellular ROS assessment, appropriate fluorescent probes were applied. Following primary incubation, the samples were incubated with corresponding secondary antibodies for 1 h at room temperature. Nuclei were

counterstained with DAPI obtained from Shanghai Aladdin Biochemical Technology (Shanghai, China). Finally, the fluorescence signals were captured and imaged using a confocal laser scanning microscope (CLSM).

ELISA

The levels of inflammatory cytokines, including IL-6, TNF-α, and IL-10, in wound tissues were quantified via immunohistochemistry (IHC) using commercial ELISA kits was purchased from Jilin Jianghe Biotechnology (Changchun, China) according to the manufacturer protocols. In brief, standards and samples were added to microtiter plates precoated with specific capture antibodies. After incubation and washing to remove unbound substances, a biotinylated detection antibody and horseradish peroxidase (HRP)-conjugated streptavidin were sequentially added. Following addition of the substrate solution for color development, the reaction was terminated and the absorbance was measured using a microplate reader at the wavelength specified. Concentrations of the target proteins in the samples were determined *via* interpolation from standard curves.

Statistical analysis

All data are presented as the mean ± standard deviation (SD). Statistical analyses were performed using GraphPad Prism software (version 9.5.1, GraphPad Software, Boston, MA, USA). Differences between groups were evaluated using one-way analysis of variance (ANOVA) followed by Tukey's multiple-comparisons test. A P value of <0.05 was considered statistically significant ($^{*}P < 0.05$, $^{**}P < 0.01$, $^{***}P < 0.001$, and $^{****}P < 0.0001$).

Results

Characterization of the nanomaterials

The physical morphology and particle size distribution of cerium-based nanomaterials were systematically evaluated using transmission electron microscopy (TEM) and dynamic light scattering (**Figure 1A–C**). According to the results, Ce@BSA, Ce@BSA-FA, and Ce@BSA-TA all exhibited a regular one-dimensional nanochain structure. This unique anisotropic growth mode indicates that the introduction of functional small-molecule ligands (FA or TA) did not destroy the self-assembly process guided by the BSA biological template. Results for the particle size distribution revealed a slight increase in the hydrodynamic diameter of Ce@BSA-FA and Ce@BSA-TA in comparison to the original Ce@BSA. This is attributed to the coating and coordination of organic molecules on the surface of the nanozymes, and confirms the occurrence of functional modification. To evaluate application potential in complex biological environments, Ce@BSA, Ce@BSA-FA, and Ce@BSA-TA were placed in water, PBS buffer and DMEM containing FBS. Stability test results after standing for 7 days (**Supplementary Figure 1**) demonstrated that the systems did not show obvious agglomeration or precipitation, and retained good colloidal dispersion. This excellent stability is mainly attributed to the steric hindrance effect provided by the BSA protein shell and the electrostatic repulsion of the surface charge. The crystal structure of the nanocomposites and the integrity of the organic framework were investigated *via* X-ray diffraction (XRD) analysis (**Figure 1D**). The experimental results showed that all samples retained a broad characteristic dispersion peak at $2\theta = 23.0°$, which is highly consistent with the peak for pure BSA protein. Together, these results indicate that the secondary structure of BSA essentially remained intact in the alkaline environment and during the mineralization reaction, and no severe denaturation or degradation occurred. In addition, the consistency of the characteristic XRD peak indicates that BSA as a biological template successfully induced orderly crystallization and nucleation of cerium ions on its peptide chain and promoted the formation of a stable organic–inorganic hybrid nanoassembly. According to results for the zeta potential (**Figure 1E**), the potential for Ce@BSA (−15.5 mV) increased to−7.41 mV for Ce@BSA-FA and −5.29 mV for Ce@BSA-TA after functionalization with FA and TA, respectively. This potential change is because of the coordination of cerium ions with carboxyl and phenolic hydroxyl groups in FA or TA molecules, resulting in surface charge shielding. Thus, the results indicate that the functional ligand was firmly anchored to the surface of the nanochains.

Fourier-transform infrared spectroscopy (FT-IR) was used to investigate chemical bonding states in the composite (**Figure 1F** and **Supplementary Figure 2**). The characteristic peak at 1612 cm^{-1} corresponds to the BSA amide I band (C=O stretching vibration), indicating the presence of the protein skeleton. For Ce@BSA-TA, a clear new absorption peak at 1714 cm^{-1} was observed, which was attributed to characteristic C=O vibration of the ester group in the TA molecule and confirms chemical incorporation of TA in the assembly [10]. Ultraviolet-visible spectroscopy (UV-Vis) absorption spectra (**Figure 1G**) provide complementary information. The characteristic BSA peak at 285 nm is derived from the conjugated system of its internal aromatic amino acids (such as tryptophan and tyrosine). The spectrum for Ce@BSA-TA exhibited a typical TA absorbance peak at 340 nm, while the spectrum for Ce@BSA-FA exhibited peak at 360 nm characteristic for the benzene-ring π–π* transition in FA (**Supplementary Figure 3**). The elemental composition of Ce@BSA-TA and the chemical valence of cerium were analyzed in depth using X-ray photoelectron spectroscopy (XPS). Full-spectrum analysis confirmed the existence of O, C, N, and S elements in the BSA protein and TA ligand in the system (**Figure 1H** and **1I**). Peak fitting for the Ce 3d high-resolution spectrum revealed multiple characteristic peaks with binding energy in the range 970–1000 eV that confirm the stable coexistence of Ce^{3+} (reduced state) and Ce^{4+} (oxidized state) in the composite [11]. On the basis of a redox-mediated catalytic mechanism, we predicted that the nanocomposite may have enzyme-like activity and therapeutic potential in addressing oxidative stress or inflammation-related diseases [12–14]. The combination of FT-IR, UV-Vis, XPS, and surface-charge results provides complementary evidence of TA coordination to

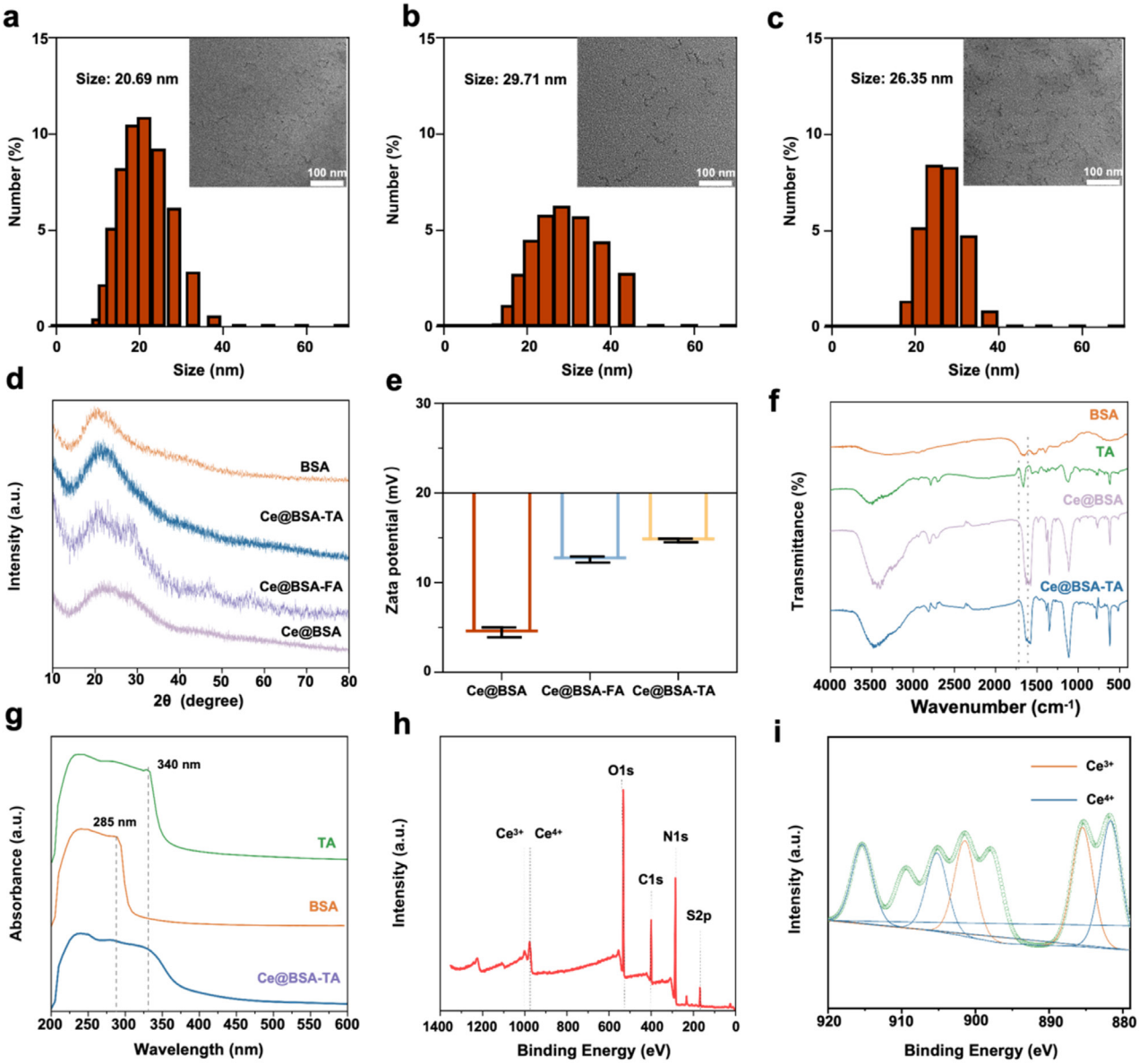


Figure 1 Characterization results. (A–C) Hydrodynamic diameter distributions and TEM images of Ce@BSA, Ce@BSA-FA, and Ce@BSA-TA. Scale bar = 100 nm. (D) XRD patterns, (E) zeta potential, (F) FT-IR spectra, and (G) UV-Vis absorption spectra for BSA, TA, and Ce@BSA-TA. (H, I) XPS analysis of (H) Ce@BSA-TA and Ce 3d peaks of Ce@BSA-TA.

the cerium-based nanochains. The characteristic TA-related absorbance and coordination-induced charge variation suggest that TA is anchored to the nanochain surface *via* metal–ligand interactions.

Radical scavenging efficiency

Hydroxyl radical (·OH) is an important factor that hinders wound transformation from a chronic inflammation state to proliferation/remodeling because of its extensive damage to key healing factors such as cells, the extracellular matrix, growth factors, and DNA [15–17]. MB colorimetric assays (**Figure 2A**) revealed that the characteristic MB absorbance peak at 664 nm was significantly attenuated under the action of ·OH generated in the Fenton reaction system; addition of the cerium-based nanomaterials (200 μg/mL) effectively suppressed this decrease in absorbance. Ce@BSA-TA exhibited significantly better ROS scavenging activity in comparison to both Ce@BSA and Ce@BSA-FA, which suggests that TA functionalization effectively improves the redox buffering capability of cerium centers *via* cooperative metal–polyphenol interactions. Quantitative analysis (**Figure 2B**) confirmed this dose-dependent scavenging activity. Ce@BSA-TA achieved a scavenging rate of 99.1 ± 0.4% at a concentration of 50 μg/mL. The synergistic effect of the TA modification was significantly better than that of FA in Ce@BSA-FA in comparison to the original Ce@BSA. As shown in **Figure 2C**, EPR spectroscopy provided direct evidence. A typical 1:2:2:1 quartet signal was measured using DMPO as the trapping agent. After Ce@BSA-TA addition, the signal intensity decayed rapidly over time and approached the baseline level within 30 min, which confirms the superior ·OH scavenging ability of this nanocomposite.

Excessive accumulation of the superoxide anion ($\cdot O_2^-$) has been observed in hyperglycemic environments [18, 19].

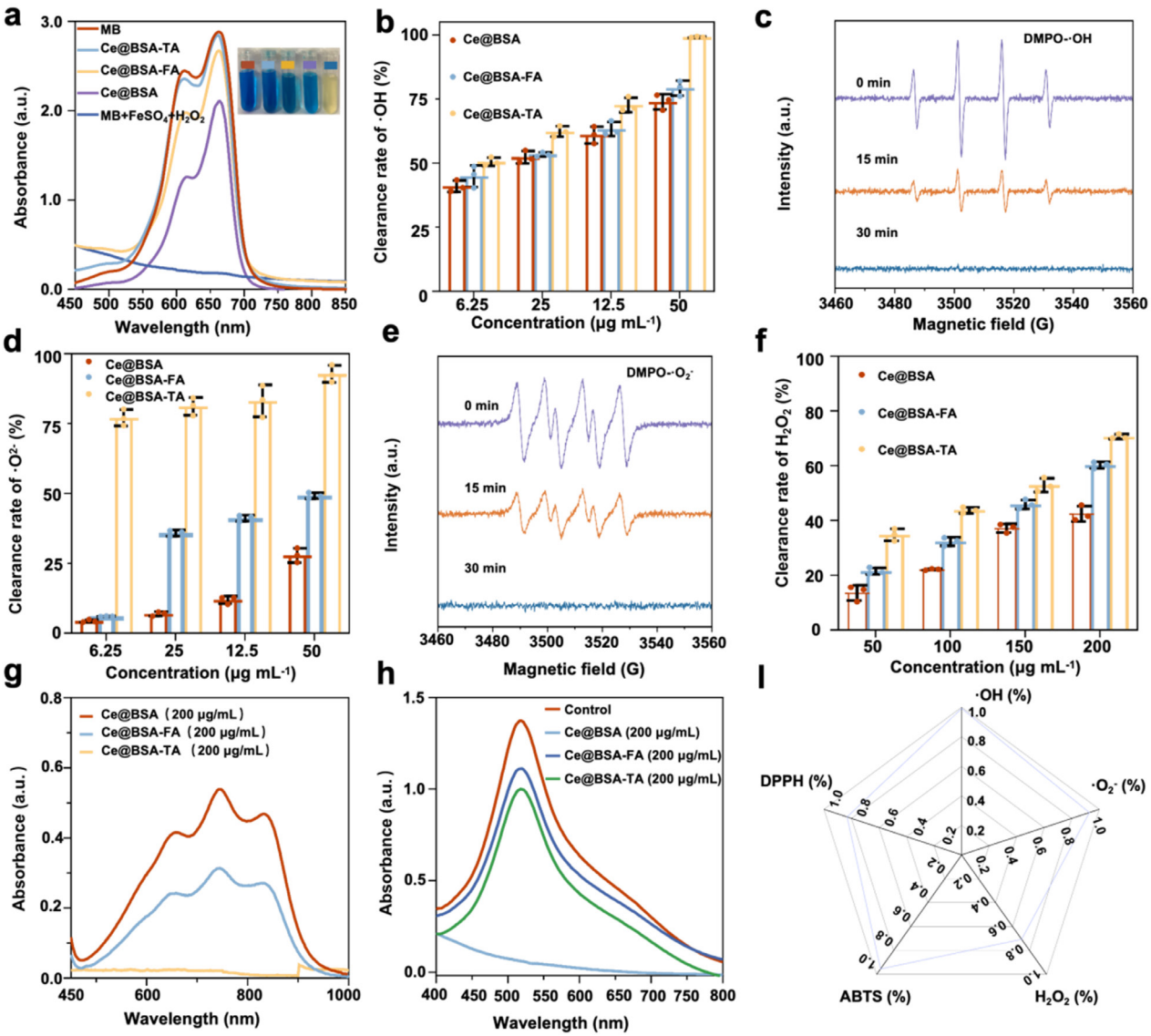


Figure 2 Evaluation of antioxidant capacity. (A) Colorimetric analysis of ·OH scavenging by MB assay. (B) ·OH scavenging activity of Ce@BSA-TA at varying concentrations. (C) EPR spectra of DMPO-trapped ·OH adducts for Ce@BSA-TA. (D) $\cdot O_2^-$ scavenging activity. (E) EPR spectra of DMPO-trapped $\cdot O_2^-$ adducts for Ce@BSA-TA. (F) H_2O_2, (G) $ABTS^{+}\cdot$, and (H) DPPH· scavenging activity. (I) Comparative analysis of radical scavenging activities.

Among the nanocomposites, Ce@BSA-TA exhibited the best scavenging performance for O_2^- (**Figure 2D**). At a concentration of 50 μg/mL, the scavenging rate reached with Ce@BSA-TA 92.8%, which was significantly higher than the rates with Ce@BSA (4.4%) and Ce@BSA-FA (49.3%). EPR monitoring (**Figure 2E**) showed that the $\cdot O_2^-$ signal was completely eliminated within 30 min, which confirms that the nanomaterial has excellent superoxide dismutase (SOD)-like activity. DO assays (**Supplementary Figure 4**) showed that Ce@BSA-TA significantly promoted the H_2O_2 decomposition to O_2 (14.27 mg/L), which represents catalase (CAT)-like activity. Ce@BSA-TA achieved scavenging efficiency of 70.65% for H_2O_2 (**Figure 2F**), which was superior to the efficiency in the two control groups. In the tests for $ABTS^{+}\cdot$ and DPPH, Ce@BSA-TA achieved almost complete scavenging at 200 μg/mL (**Figure 2G** and **2H, Supplementary Figures 5** and **6**). In addition, its activity did not significantly decrease after 2 months of standing (**Supplementary Figure 7**), which demonstrates the long-term stability of its performance. The overall antioxidant performance and reducing power of the materials were evaluated in terms of Fe-TPTZ reduction and the Prussian blue reaction with potassium ferricyanide. The results showed that Ce@BSA-TA exhibited the strongest electron donor capability, and efficiently reduced Fe^{3+} complexes (**Supplementary Figure 8**). A radar chart was used to visually compare the comprehensive antioxidant performance of the cerium-based nanomaterials in terms of their scavenging efficiency for five typical free radicals (**Figure 2I**).

Evaluation of ROS scavenging

To evaluate the potential of the cerium-based nanocomposites as antioxidant therapeutics, we first investigated their ROS scavenging ability *in vitro*, and then assessed their cellular biocompatibility.

As cerium-based nanomaterials possess SOD-like and CAT-like activities, we evaluated the intracellular ROS scavenging

efficacy of Ce@BSA, Ce@BSA-FA, and Ce@BSA-TA at the cellular level using DCFH-DA fluorescence staining assays. As shown in **Figure 3A**, no fluorescence signal was observed for the PBS control group without H_2O_2 treatment, which indicates that L929 cells maintain a low level of endogenous ROS under normal physiological conditions. On stimulation with H_2O_2, the excellent transmembrane permeability of the materials resulted in the production of a large amount of intracellular ROS, with strong green fluorescence observed within the cells. Tests using different concentrations of the cerium-based nanomaterials revealed a significant concentration-dependent decay in intracellular fluorescence intensity. When the concentration was increased to 12.5 μg/mL, the fluorescence signals essentially recovered to baseline levels in all groups, which confirms the excellent antioxidant activity and intracellular ROS scavenging ability of the three materials. Comparative analysis revealed that at the same treatment concentration, weakest fluorescence signal was observed for treatment with Ce@BSA-TA, which indicates its optimal effect in downregulating intracellular ROS.

The intracellular oxygen production of cerium-based nanocomposites was directly assessed using the oxygen-sensitive probe $[Ru(dpp)_3]Cl_3$ [20]. As shown in **Figure 3B**, the PBS control group exhibited strong red fluorescence, indicating a relatively hypoxic microenvironment within the cells. In the H_2O_2-only treatment group, the fluorescence intensity decreased only slightly because of slow endogenous decomposition of H_2O_2. By contrast, the fluorescence intensity for the nanomaterial-treated experimental group was significantly weakened, with a clear concentration dependence evident. In particular, at a concentration of 12.5 μg/mL, probe fluorescence in the Ce@BSA-TA group was essentially quenched. This phenomenon is attributed to the excellent CAT activity of Ce@BSA-TA, with efficient catalysis of intracellular H_2O_2 conversion to O_2 that leads to fluorescence quenching of the oxygen-sensitive probe by increasing the intracellular oxygen content. This result indirectly confirms the ability of the material to efficiently consume H_2O_2 intracellularly.

Systematic evaluation of the biosafety of cerium-based nanochains

After verifying the intracellular ROS-scavenging and oxygen production capabilities of the cerium-based nanocomposites, we systematically evaluated their biosafety. The effects of the different materials on the morphology and viability of L929 cells were observed using live/dead fluorescence staining (**Figure 4A**). Cells in all the treatment groups exhibited dense green fluorescence (live cells),

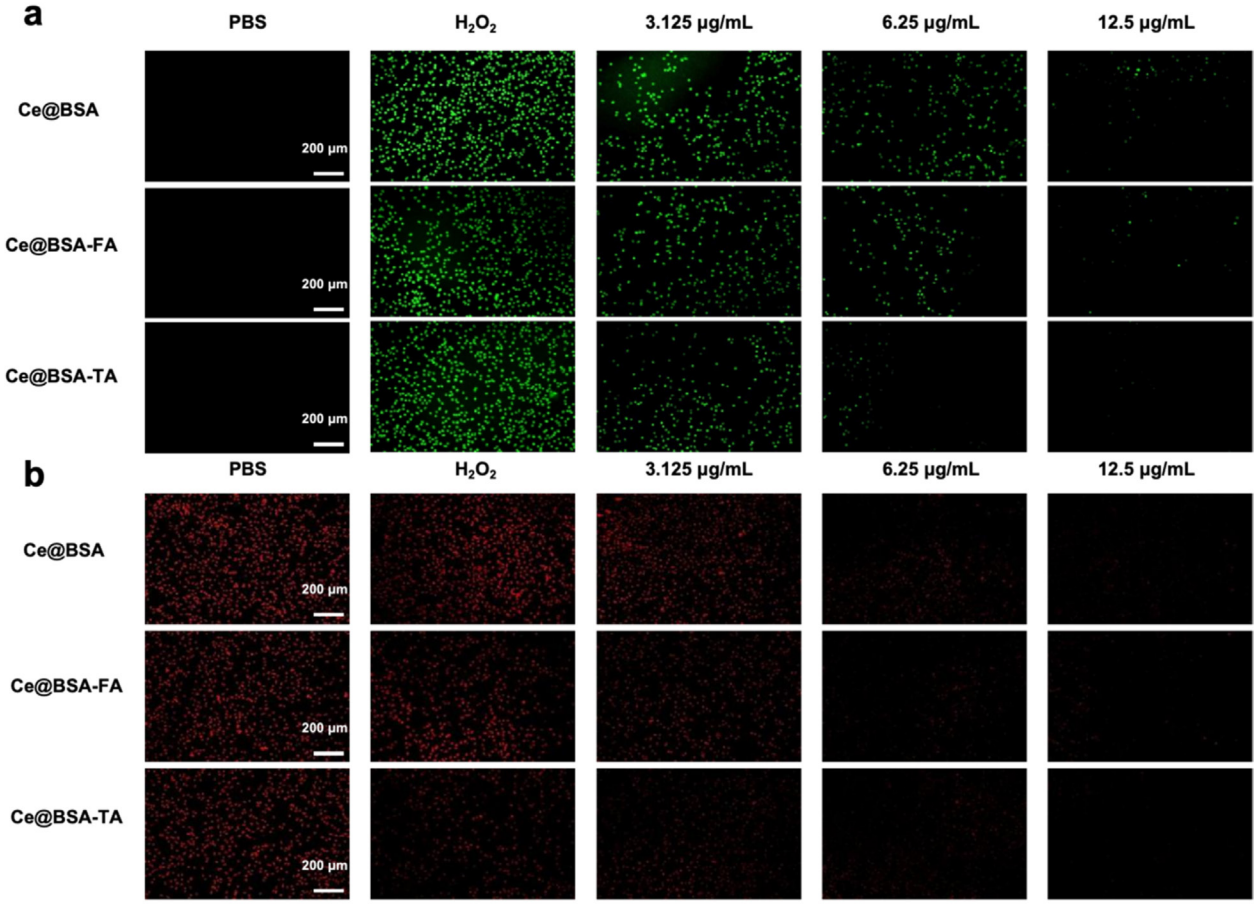


Figure 3 *In vitro* evaluation of Ce-based nanochains on L929 cells. (A) Representative CLSM images showing intracellular ROS levels visualized *via* DCFH-DA staining (green) following H_2O_2 treatment. (B) CLSM visualization of intracellular oxygenation mediated by nanozymes using an oxygen-sensitive probe, and the H_2O_2 scavenging capability. Data are presented as the mean ± SD (n = 3). Scale bars = 200 μm.

with virtually no red fluorescence representing dead cells, and maintained a good spindle-shaped adherent state, which provided preliminary confirmation of the good cell compatibility of the materials. We then quantitatively evaluated the cytotoxic effects of Ce@BSA-TA on NIH 3T3 and L929 cells using a CCK-8 assay (**Figure 4B** and **4C**). Data showed that even after co-culturing at a high concentration of 300 μg/mL for 24 h, cell viability remained stable at >90%, and the cells exhibited a normal proliferation trend over time, which confirmed the extremely low cytotoxicity of the nanomaterials. To assess the safety of blood contact after local administration, we also measured the hemolytic properties of the materials (**Figure 4D** and **4E**). The supernatant after centrifugation remained transparent for all concentration groups, and plots of the hemolysis rate showed no significant fluctuations at the characteristic absorption peak of hemoglobin. Quantitative calculations showed that even at a concentration as high as 600 μg/mL, the hemolysis rate was still far below the safety threshold of 5%, which indicates excellent blood compatibility. Finally, the skin irritative properties of Ce@BSA-TA were assessed in skin sensitization tests (**Figure 4F**). The photos show that after 15 days of coverage at different Ce@BSA-TA concentrations, the skin surface was smooth and no allergic reactions such as redness, swelling, erythema, or desquamation were observed, which confirms the tissue safety of this material when topically applied for skin wound repair.

Therapeutic potential in a diabetic mouse model of skin wounds

Inspired by the *in vitro* experimental results, we evaluated the therapeutic potential of Ce@BSA-TA in a diabetic mouse model of skin wounds. As shown in **Figure 5A**, a diabetic model was established *via* STZ induction, and a full-thickness skin excision lesion was prepared on the back

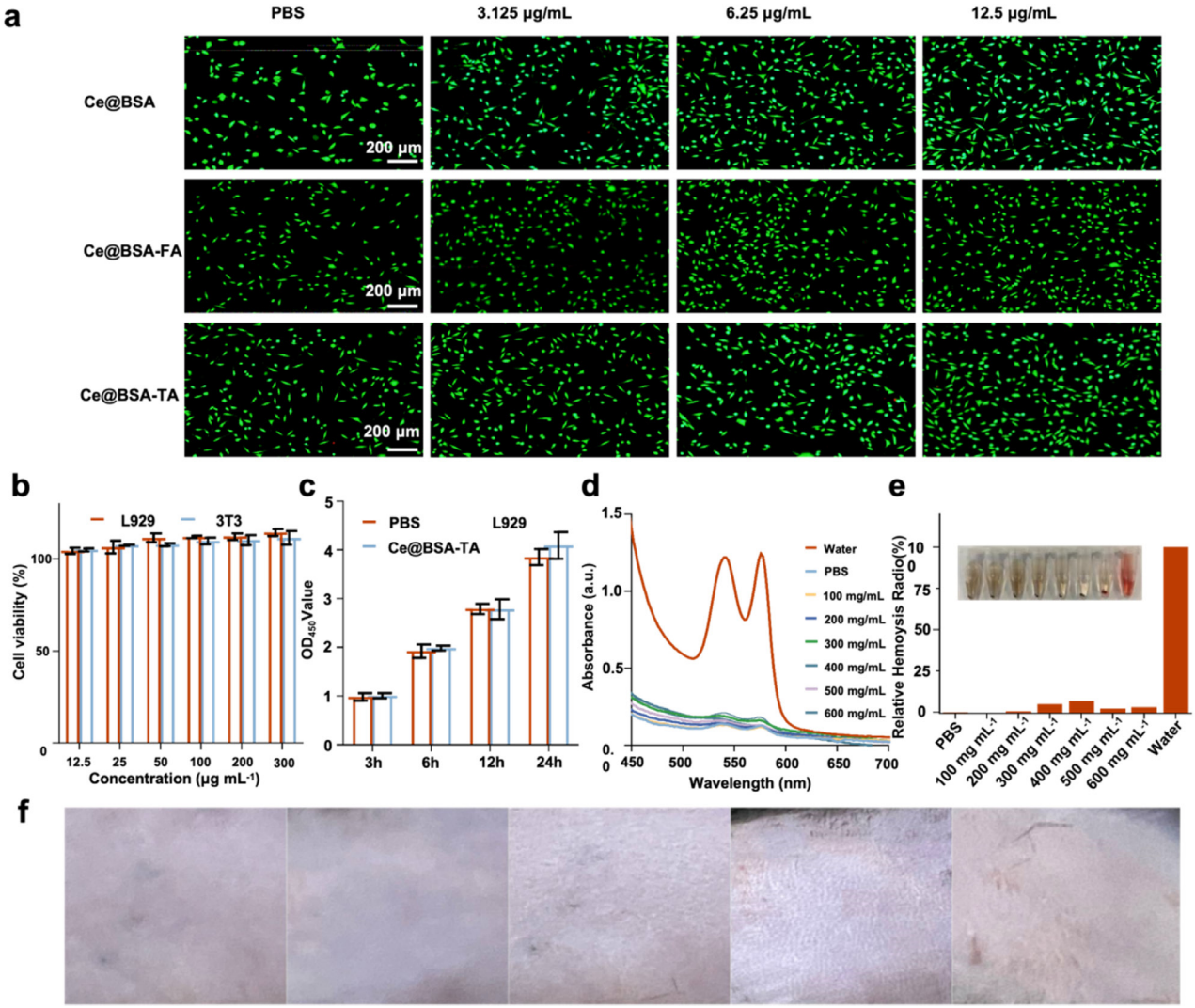


Figure 4 *In vitro* and *in vivo* biocompatibility evaluations of Ce-based nanochains. (A) Live/dead staining images of L929 cells after 24 h of incubation with the materials specified (green: live cells, red: dead cells). Scale bars = 200 μm. (B) Cytotoxicity of Ce@BSA-TA at varying concentrations against NIH 3T3 and L929 cells. (C) Time-dependent cell viability of L929 cells treated with Ce@BSA-TA, assessed *via* CCK-8 assay. (D) Hemolysis curves and (E) relative hemolysis ratios for RBCs treated with different Ce@BSA-TA concentrations (the inset in D shows centrifuged samples). (F) Representative photographs showing skin sensitization assessment following application of different Ce@BSA-TA concentrations.

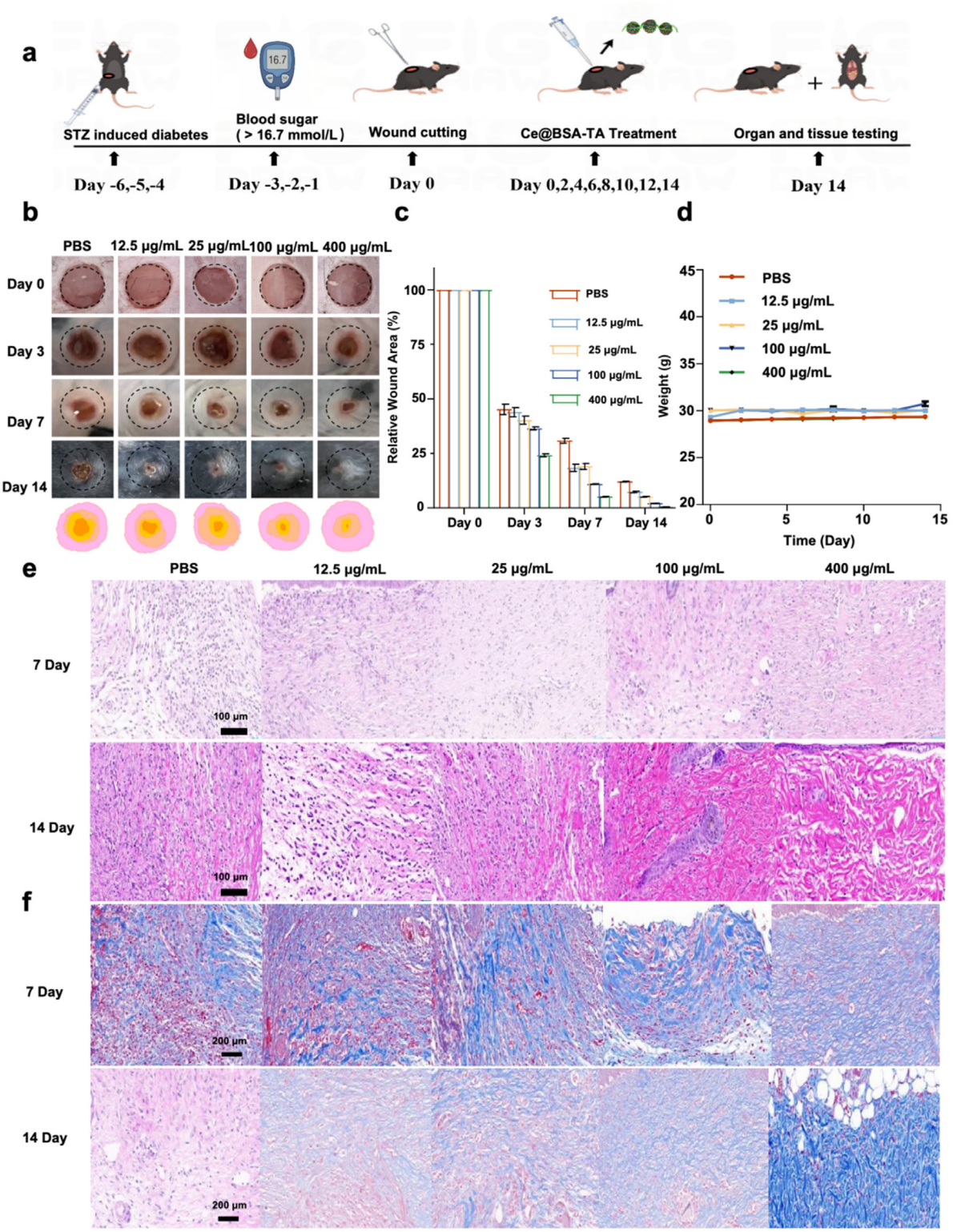


Figure 5 *In vivo* therapeutic efficacy of Ce@BSA-TA for diabetic wound healing. (A) Schematic illustration of the experimental timeline for diabetes induction, wound creation, Ce@BSA-TA treatment, and subsequent tissue analysis. (B) Representative photographs of full-thickness skin wounds in diabetic mice treated with different Ce@BSA-TA concentrations over 14 days, with schematic representations of the remaining wound area shown below. (C) Quantitative analysis of the relative wound area on days 0, 3, 7, and 14 after treatment. (D) Body-weight changes in diabetic mice during the treatment period. (E) Representative H&E-stained sections of wound tissues collected on days 7 and 14 (scale bar = 100 μm). (F) Representative Masson's trichrome–stained sections of wound tissues collected on days 7 and 14 (scale bar = 200 μm).

of the animals to simulate chronic wounds [21]. Dynamic monitoring results for wound repair (**Figure 5B** and **5C**) revealed that Ce@BSA-TA has significant pro-healing bioactivity. During the treatment period, the difference in wound closure rates between the treatment groups and the PBS control group gradually widened over time, and a clear dose–response relationship was evident. On day 7 of treatment, the residual wound area was significantly smaller in

the group treated with a high concentration (400 μg/mL) than in the other groups; by day 14, wounds in this group had essentially achieved clinical healing. By contrast, although the 100-μg/mL group showed better healing than the control group, the rate was still inferior to that in the high-concentration group, which demonstrates that Ce@BSA-TA accelerates wound repair in a concentration-dependent manner. Furthermore, the body weight of mice in each group remained stable during the experiment (**Figure 5D**), with no significant fluctuations observed. To evaluate the systemic biosafety of Ce@BSA-TA, H&E histological analysis of the major organs (heart, liver, spleen, lung, and kidney) of mice was performed after day 14 of treatment (**Supplementary Figure 9**). For the staining of major organ tissues, the heart, liver, spleen, lungs, and kidney tissue samples were fixed in paraformaldehyde solution overnight, followed by paraffin embedding and paraffin section preparation. Subsequent staining procedures were consistent with those used for wound tissue staining. The results showed no obvious pathological damage or inflammatory response in the major organs of any treatment group. Together, the body-weight data and organ section results demonstrate that this treatment regimen has excellent biosafety in the repair of chronic diabetic wounds, with no systemic toxicity.

Histological evaluation further revealed the characteristics of wound regeneration. H&E staining of the wound (**Figure 5E**) showed that by day 14, both the control and low-concentration groups still exhibited significant inflammatory-cell infiltration and a disordered distribution of fibroblasts, which indicated that wound healing was stalled at the inflammatory stage. In stark contrast, a very strong anti-inflammatory effect was observed in the group treated with 400 μg/mL, with a significant reduction in the number of inflammatory cells, and the presence of spindle-shaped, tightly arranged fibroblasts in the newly formed dermis. Masson staining (**Figure 5F**) confirmed the enhancement of collagen remodeling. By day 14, the high-concentration group showed a large number of deep blue, densely networked bundles of mature collagen fibers in the wound tissue, while the control group showed only sparse, discontinuous collagen deposition. To summarize, Ce@BSA-TA significantly accelerated the closure of diabetic chronic wounds and of tissue regeneration by efficiently regulating the wound microenvironment, inhibiting inflammatory responses induced by oxidative stress, and promoting redirection of collagen deposition.

Effects on remodeling of the immune microenvironment

To elucidate the mechanism underlying promotion of wound healing by the cerium-based nanocomposites, we first investigated their effect on remodeling of the immune microenvironment. Experimental results showed that the cerium-based nanocomposites could significantly regulate the polarization behavior of macrophages. Immunofluorescence staining revealed that expression levels of the M1 marker CD86 in wound tissue were significantly downregulated on days 7 and 14, while the fluorescence intensity of the M2 marker CD206 increased in a concentration-dependent manner (**Figure 6A**), which suggests that the nanocomposites effectively promoted macrophage transformation to the M2 phenotype [22]. Quantitative analysis confirmed that the nanomaterial significantly inhibited the release of pro-inflammatory factors TNF-α and IL-6, and simultaneously upregulated levels of the anti-inflammatory factor IL-10 (**Figure 6B** and **6C**). This precise regulation of the balance of immune factors transformed the wound microenvironment from a pro-inflammatory to an anti-inflammatory state conducive to repair.

Induction of vascular regeneration

We then investigated whether the improvement in wound microenvironment could induce angiogenesis. IHC staining of wound tissue revealed expression trends for anti inflammatory and pro-inflammatory factors after cerium-based nanochain treatment that were highly consistent with the previous quantitative results (**Figure 7A–C**) and reflect favorable conditions for angiogenesis. IHC analysis confirmed significantly enhanced activation of the VEGF pathway after nanochain treatment, manifest as a marked increase in VEGF protein expression, which directly led to an increase in levels of the endothelial cell marker CD31 (**Figure 7D** and **7E**). Continuous observation on days 7 and 14 revealed the formation of a denser mature vascular network, which we attribute to a reaction cascade from anti-inflammation to pro-repair that provides a solid biological basis for efficient healing of chronic wounds such as those in diabetes.

Conclusion

We prepared three cerium-based nanomaterials *via* BSA mineralization and functionalized them with FA and TA ligands. Testing revealed that all three cerium-based nanomaterials can scavenge ROS such as ·OH and $\cdot O_2^-$ and free radicals such as $ABTS^{+}\cdot$ and DPPH·. The TA-functionalized cerium-based material exhibited relatively better scavenging ability, along with SOD-like and CAT-like enzyme activities. *In vitro* cell experiments confirmed that Ce@BSA-TA exhibited good free-radical scavenging and CAT activity. Cytotoxicity experiments (calcein-AM/PI, CCK-8 and MTT) further demonstrated that the cerium-based nanomaterials had no significant toxicity and had a concentration-dependent proliferative effect. Hemolysis and skin allergy experiments verified the good biocompatibility and favorable toxicity. *In vivo* experiments using a mouse model of diabetic wounds showed that Ce@BSA-TA can effectively inhibit inflammatory responses, accelerate fibroblast hyperplasia and collagen deposition, and promote epidermal regeneration. ROS fluorescence staining and immunofluorescence analysis showed that high Ce@BSA-TA concentrations effectively reduced ROS levels in the wound, inhibited the expression of M1 macrophage markers (CD86, IL-6, TNF-α), and upregulated M2 macrophage markers (CD206, IL-10) and pro-angiogenic factors (CD31, VEGF). After 14

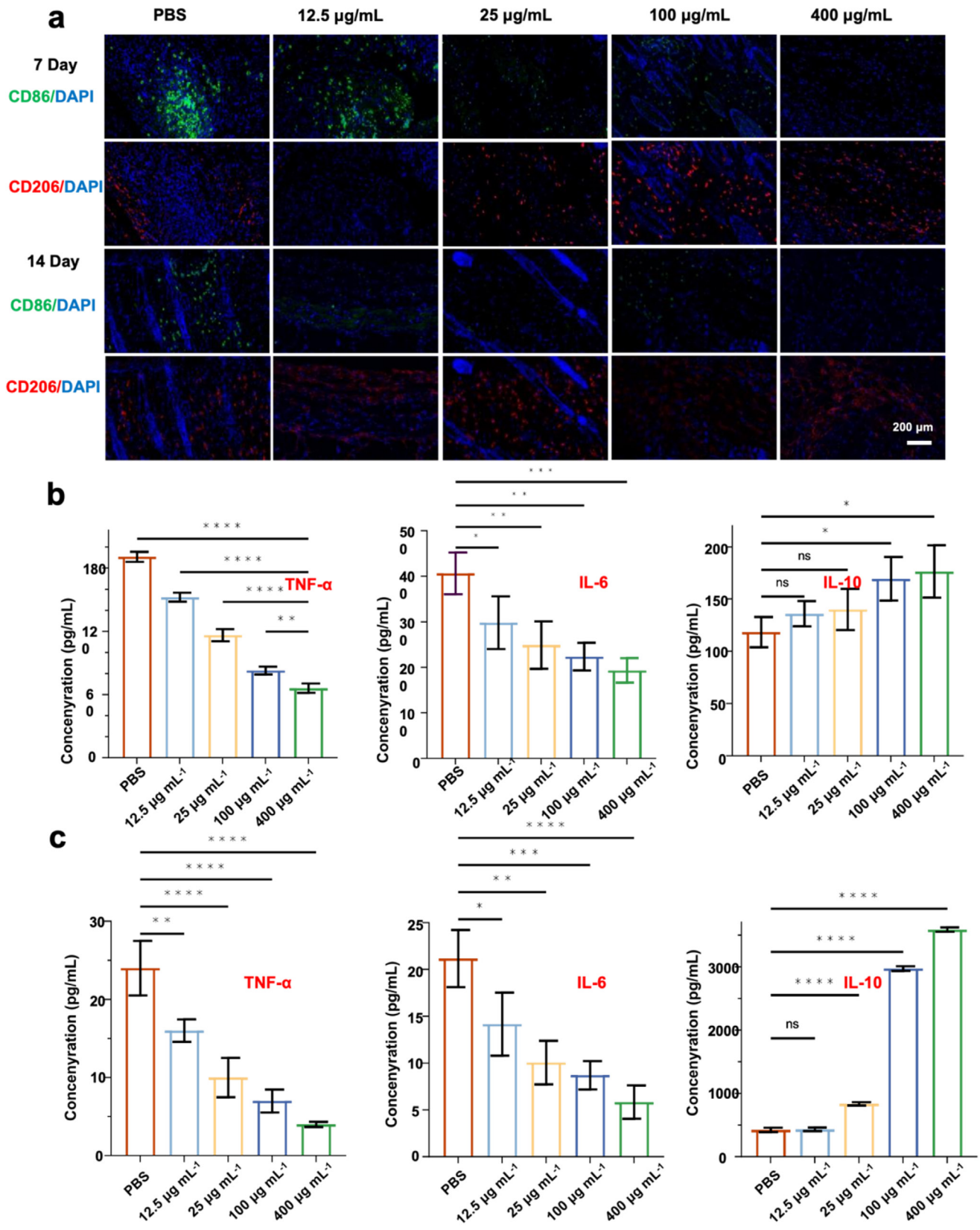


Figure 6 Evaluation of the immunomodulatory effects of Ce@BSA-TA on macrophage polarization and inflammatory cytokine expression in diabetic wound tissues. (A) Representative immunofluorescence images of wound sections collected on days 7 and 14 after treatment and stained for the M1 macrophage marker CD86 (green) and the M2 macrophage marker CD206 (red). Nuclei were counterstained with 4′,6-diamidino-2-phenylindole (DAPI; blue). Scale bar = 200 μm. (B, C) Quantitative analysis of concentrations of the pro-inflammatory cytokines TNF-α and IL-6 and the anti-inflammatory cytokine IL-10 in wound tissues on (B) day 7 and (C) day 14 as determined by ELISA. Data are presented as the mean ± SD (n = 3 biologically independent mice per group at each time point). Statistical significance is indicated as **P* < 0.05, ***P* < 0.01, ****P* < 0.001, and *****P* < 0.0001; ns, not significant.

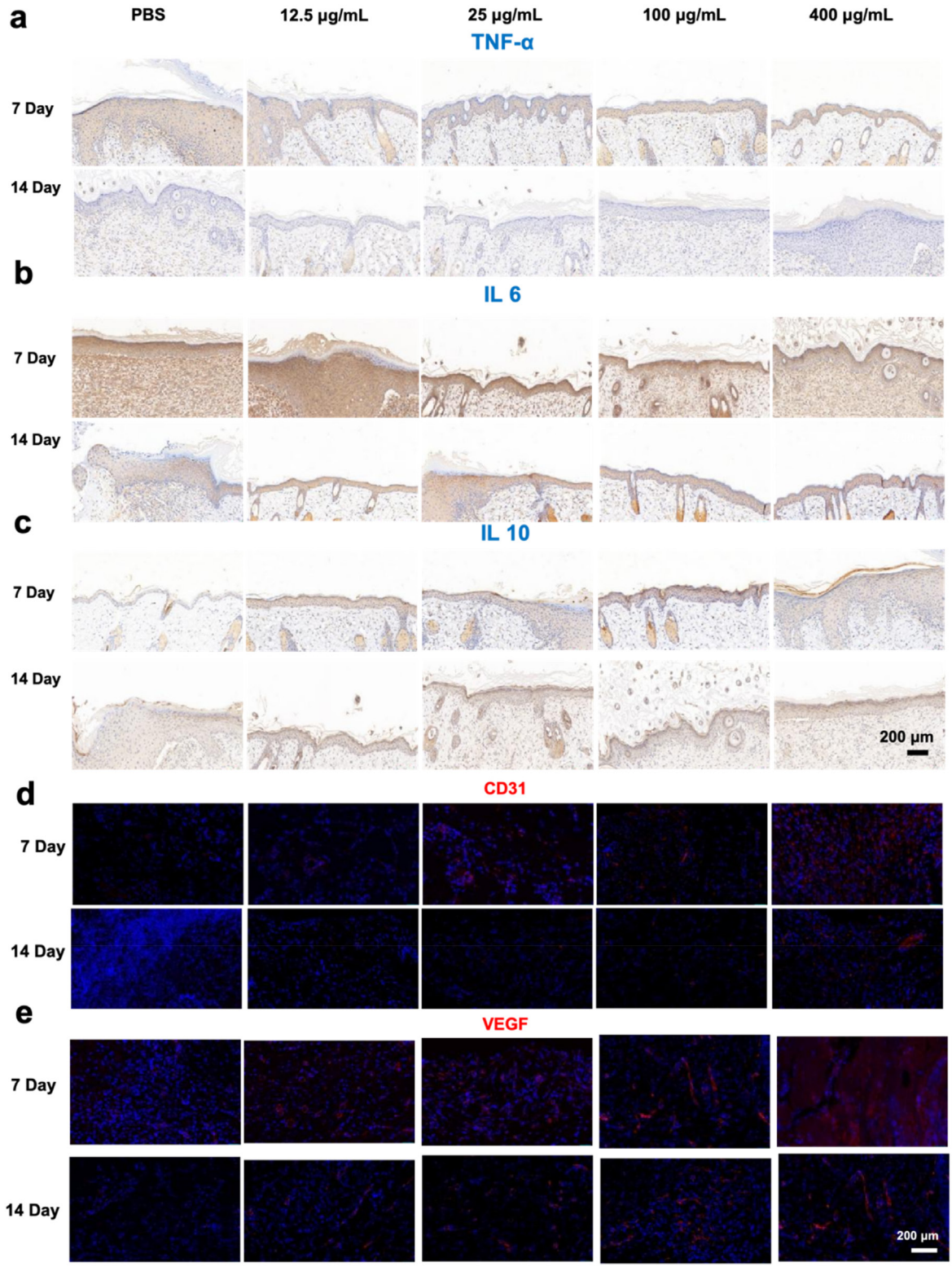


Figure 7 Histological analysis of inflammatory microenvironment remodeling and pro-angiogenic performance mediated by Ce-based nanochains. (A–C) Representative IHC stained images showing expression levels of (A) TNF-α, (B) IL-6, and (C) IL-10 (C) in regenerated skin tissues at day 7 and day 14. (D, E) Representative immunofluorescence images of wound sections at different time points after staining for angiogenic markers (D) CD31 and (E) VEGF. Data are presented as the mean ± SD (n = 3). Scale bar = 200 μm.

days of treatment, diabetic wounds in this model had almost completely healed, with no pathological damage to internal organs, which indicates that the Ce@BSA-TA nanozyme has good biocompatibility. Our study confirms the significant advantages of polyphenol-functionalized cerium-based nanomaterials in scavenging ROS *via* multiple pathways and in regulating macrophage polarization. It also lays a theoretical and experimental foundation for the development

of novel antioxidant metalloenzyme biomaterials and their application in skin tissue engineering.

Data availability statement

The data supporting the findings of this study are available from the corresponding author on reasonable request.

Ethics statement

All animal experimental procedures were performed in accordance with relevant institutional guidelines for the care and use of laboratory animals and were approved by the Institutional Animal Care and Use Committee of Jilin Medical University (approval no. 2025-LW004).

Author contributions

Yuhui Sun, Yan Xu and Hongda Ma: Conceptualization, methodology, investigation, formal analysis, and writing–original draft. Yuan Cui and Xiangru Feng: Investigation, validation, and data curation. Xincui Shi and Alexander A. Titov: Methodology and formal analysis. Leijiao Li and Wenliang Li: Supervision, project administration, funding acquisition, and writing–review and editing. All the authors have read and approved the final manuscript.

Funding

Financial support from the Jilin Province Science & Technology Committee (grant no. 20260205018GH), a Jilin Provincial Doctoral Research Fellowship (BST202530), and a Jilin Provincial Department of Education Science and Technology Research Project (no. JJKH20262240BS) is acknowledged.

Acknowledgments

The authors acknowledge Jilin Medical University for technical assistance.

Conflict of interest

The authors declare that they have no known competing financial interests or personal relationships that could have appeared to influence the work reported in this paper.

Supplementary material

Supplementary material can be downloaded from https://bio-integration.org/wp-content/uploads/2026/10/bioi20260136_Supplemental.pdf.

References

[1] Unnikrishnan R, Shaw JE, Chan JCN, Wild SH, Peters AL, et al. Prediabetes. Nat Rev Dis Primers 2025;11(1):49. [PMID: 40676018 DOI: 10.1038/s41572-025-00635-0]

[2] Xu Z, Yang W, Zhang R, Zhang G, Liang X, et al. Microenvironment-programmed siRNA-based hydrogel for spatiotemporal gene silencing in wound healing. Adv Mater 2025;37(47):e09558. [PMID: 40913576 DOI: 10.1002/adma.202509558]

[3] Zhang Y, Zhang W, Wang W, Zhao X, Wang X. TiO/CIP/SilMA hydrogels promote the repair of infected wounds by interfering with bacterial signaling and energy metabolism. Cell Biomater 2026;2(3):100217. [DOI: 10.1016/j.celbio.2025.100217]

[4] Wang W, Gui H, Wei X, Liu H, Wang X. Cuproptosis to cuproptosis-like: therapeutic strategies for bacterial infection. Adv Mater 2025;37(37):e2506119. [PMID: 40538266 DOI: 10.1002/adma.202506119]

[5] Li S, Susztak K. Mitochondrial dysfunction has a central role in diabetic kidney disease. Nat Rev Nephrol 2025;21(2):77-8. [PMID: 39681602 DOI: 10.1038/s41581-024-00919-w]

[6] Li H, Wei S, Ling Q, Wang R, Liu T, et al. Nanozyme-reinforced hydrogel spray as a reactive oxygen species-driven oxygenator to accelerate diabetic wound healing. Adv Mater 2025;37(34):e2504829. [PMID: 40492891 DOI: 10.1002/adma.202504829]

[7] Liu S, Chen H, Xu Y, Li L, Shi X, et al. Cascade catalytic nanozyme platform for combined antibacterial, anti-inflammatory, and pro-healing therapy of infected diabetic wounds. J Nanobiotechnology 2026;24(1):128. [PMID: 41639675 DOI: 10.1186/s12951-026-04052-7]

[8] Lu L, Liao J, Xu C, Xiong Y, Zhou J, et al. Kinsenoside-loaded microneedle accelerates diabetic wound healing by reprogramming macrophage metabolism via inhibiting IRE1α/XBP1 signaling axis. Adv Sci 2025;12(26):e2502293. [PMID: 40279546 DOI: 10.1002/advs.202502293]

[9] Li Z, Li Y, Zhang Z, Cui H, Ji X, et al. Physicochemical dual cross-linked multifunctional conductive organohydrogel sensors for fireworks burn wound healing and intelligent real-time monitoring. Polym Sci Technol 2025;1(3):245-60. [PMID: 42257191 DOI: 10.1021/polymscitech.4c00018]

[10] Wang Z, Wang ZX, Xu KF, An Y, Cui M, et al. A metal-polyphenol-based antidepressant for alleviating colitis-associated mental disorders. Adv Mater 2025;37(3):e2410993. [PMID: 39623787 DOI: 10.1002/adma.202410993]

[11] Fu H, Wang Y, Huang B, Liang Z, Li Y, et al. Tannic acid-cerium nanoenzymes serve as broad-spectrum antioxidants to alleviate acute kidney injury by modulating macrophage polarization, mitophagy and endoplasmic reticulum stress. J Control Release 2025;380:892-909. [PMID: 39971251 DOI: 10.1016/j.jconrel.2025.02.038]

[12] Han Z, Chen Q, Duan X, He Z, Mou N, et al. Targeting engineered cell membrane camouflaged gallic acid-cerium nanozyme for intercepting the inflammation-free radical vicious cycle in atherosclerosis. J Nanobiotechnology 2026;24(1):339. [PMID: 41781992 DOI: 10.1186/s12951-026-04230-7]

[13] Liu D, Lu G, Shi B, Ni H, Wang J, et al. ROS-scavenging hydrogels synergize with neural stem cells to enhance spinal cord injury repair

via regulating microenvironment and facilitating nerve regeneration. Adv Healthc Mater 2023;12(18):e2300123. [PMID: 36989238 DOI: 10.1002/adhm.202300123]

[14] Gu H, Li J, Dai P, Sun T, Chen C, et al. Polyphenol oxidase-like nanozymes. Adv Mater 2025;37(43):e09346. [PMID: 40847695 DOI: 10.1002/adma.202509346]

[15] Bao S, Yu D, Tang Z, Wu H, Zhang H, et al. Conformationally regulated "nanozyme-like" cerium oxide with multiple free radical scavenging activities for osteoimmunology modulation and vascularized osseointegration. Bioact Mater 2024;34:64-79. [PMID: 38186961 DOI: 10.1016/j.bioactmat.2023.12.006]

[16] Zhu Z, Ding J, Qin M, Wang L, Jiang D, et al. Enhanced ·OH-scavenging activity of Cu-CeOx nanozyme via resurrecting macrophage Nrf2 transcriptional activity facilitates diabetic wound healing. Adv Healthc Mater 2024;13(12):e2303229. [PMID: 38298062 DOI: 10.1002/adhm.202303229]

[17] Yan Z, Zhang Y, Chen Q, Li J, Ning X, et al. Carbon dot superoxide dismutase nanozyme enhances reactive oxygen species scavenging in diabetic skin wound repair. J Adv Res 2026;79:691-706. [PMID: 40154736 DOI: 10.1016/j.jare.2025.03.049]

[18] Cai X, Huang M, Qiu W, Xie X, Wu J, et al. Nanoparticles selectively regulate the generation and scavenging of multiple reactive oxygen species at designated locations and states. J Am Chem Soc 2025;147(25):21385-99. [PMID: 40512018 DOI: 10.1021/jacs.4c17687]

[19] Jing Y, Deng Z, Yang X, Li L, Gao Y, et al. Ultrathin two-dimensional polydopamine nanosheets for multiple free radical scavenging and wound healing. Chem Commun (Camb) 2020;56(74):10875-8. [PMID: 32940278 DOI: 10.1039/d0cc02888f]

[20] Wang X, He M, Zhao Y, He J, Huang J, et al. Bimetallic PtPd atomic clusters as apoptosis/ferroptosis inducers for antineoplastic therapy through heterogeneous catalytic processes. ACS Nano 2025;19(48):41418. [PMID: 41277105 DOI: 10.1021/acsnano.5c18495]

[21] Wang N, Mu W, Kolesnik IA, Potkin VI, Li L, et al. A self-oxygenating nanozyme cascade system for drug-resistant bacterial infected diabetic wound healing. ACS Appl Mater Interfaces 2025;17(47):64967-79. [PMID: 41217211 DOI: 10.1021/acsami.5c20613]

[22] Cui S, Meng S, Liu Y, Chen S, Hu W, et al. Activating ferroptosis of M1 macrophages: a novel mechanism of asiaticoside encapsuled in GelMA for anti-inflammation in diabetic wounds. Exploration (Beijing) 2025;5(6):20240062. [PMID: 41476651 DOI: 10.1002/EXP.20240062]